Characterizations of Two-Dimensional Materials with Cryogenic Ultrahigh Vacuum Near-Field Optical Microscopy in the Visible Range

Jeremy F. Schultz [1,a)] and Nan Jiang [2,b)]

[1]Nanoscale Spectroscopy Group, Physical Measurement Laboratory, National Institute of Standards and Technology, Gaithersburg, Maryland 20899, USA
[2]Department of Chemistry, University of Illinois Chicago, Chicago, Illinois 60607, USA

[a)] Electronic mail: jeremy.schultz@nist.gov

[b)] Electronic mail: njiang@uic.edu

The development of new characterization methods has resulted in innovative studies of the properties of two-dimensional (2D) materials. Observations of nanoscale heterogeneity with scanning probe microscopy methods have led to efforts to further understand these systems and observe new local phenomena by coupling light-based measurement methods into the tip–sample junction. Bringing optical spectroscopy into the near field in ultrahigh vacuum at cryogenic temperatures has led to highly unique studies of molecules and materials, yielding new insight into otherwise unobservable properties nearing the atomic scale. Here we discuss studies of 2D materials at the subnanoscale where the measurement method relies on the detection of visible light scattered or emitted from the scanning tunneling microscope (STM). We focus on tip-enhanced Raman spectroscopy (TERS), a subset of scattering-type scanning near-field optical microscopy (s-SNOM), where incident light is confined and enhanced by a plasmonic STM tip. We also mention scanning tunneling microscope induced luminescence (STML), where the STM is used as a highly local light source. The measurement of light–matter interactions within the atomic STM cavity is expected to continue to provide a highly useful platform to study new materials.

I. INTRODUCTION

The ability to understand the behavior of materials hinges on the ability to measure lattice structures and properties with relevant spatial resolution. Improvements to measurement methods and the development of new instrumentation have led to studies of materials with respect to increasingly local interactions or phenomena.[1] At the surface or interface of materials, dimensional confinement can lead to new or exotic properties that can be highly localized. This becomes especially relevant in the case of atomically thin layers,[2] or two-dimensional (2D) materials.[3] As a result, a thorough understanding of this class of materials requires a highly sensitive characterization method with nanoscale or angstrom-scale spatial resolution.

Since the discovery of graphene in 2004,[4] 2D materials, have attracted considerable attention due to their unique electronic, optical, and mechanical properties that arise within atomically thin sheets.[5, 6] The ever-increasing library of 2D materials and more recently van der Waals heterostructures[7] requires the ability to observe relevant phenomena with a high level of sensitivity with respect to atomic-scale landscapes.[8] In this manner, the ongoing development of new characterization methods is essential to realizing the full potential of both new and established materials.[9] The situation becomes further complicated when systems exhibit nanoscale heterogeneity or local disorder and phenomena,[10] which can only be captured by measurements with a high degree of spatial resolution.

The invention of the scanning probe microscope (SPM), specifically the scanning tunneling microscope (STM), enabled the ability to image the electronic structure and atomic lattice of surfaces in real-space.[11] As a result, the SPM quickly came to revolutionize our understanding of surfaces and interfaces. Within the STM, an

atomically sharp metallic probe or tip is brought very close to a conductive or semiconductive sample. When the probe is terminated in a single apex atom, it becomes possible to image a surface with atomic resolution. A voltage bias is applied between the sample and the tip resulting in the flow of electrons (tunneling current). This tunneling current is exceedingly sensitive to the local density of states (LDOS) of the surface at the position of the tip.[12] Subsequently, STM images can capture a mixture of topological and electronic information. And so, the tip–sample junction becomes a rich source of local information that can be used to image materials by raster scanning the probe tip across the surface. However, stability of the tip–sample junction is essential, and so many STMs rely upon ultrahigh vacuum (UHV) and cryogenic temperatures. Such implementations have resulted in studies that provide unprecedented images of molecules and materials at the atomic-scale, resolving individual molecules, atoms, and even bonds.[13]

By contrast, traditional imaging and spectroscopic methods that rely on light are diffraction-limited according to the Abbe diffraction limit, where the resolving distance is roughly proportional to $\frac{\lambda}{2}$, where λ is the wavelength of light used to image a sample.[14] SPM circumvents this limit by relying on the interaction between an ideally atomically sharp probe tip and a sample to yield images with subnanoscale resolution. Some efforts have found success in using the SPM probe to either confine light into the near-field or alternatively locally induce photon emission or measure the effects of light absorption.[15] Although initially proposed in 1928 by Edward Synge,[16] near-field optical microscopy was fundamentally limited by contemporaneous technology and has only recently become a viable method to characterize low-dimensional materials at the nanoscale and beyond due to significant technical developments. In 1972, Ash and Nicholls realized

super-resolution aperture scanning microscopy with a microwave experiment where they were able to resolve a grating with a line width of $\frac{\lambda}{60}$ by relying on a subwavelength-sized aperture in a diaphragm.[17] Slightly later efforts by Pohl in 1984 would use illumination through a hole in a probe tip to image a grating with 488 nm radiation demonstrating a resolving power of at least $\frac{\lambda}{20}$.[18] Based on these early demonstrations, many early efforts focused on illumination through a probe with an aperture to overcome the diffraction limit in optical microscopy. Pohl, a pioneer in scanning near-field optical microscopy (SNOM), has previously published some remarks[19] and a review[20] that provide a fascinating account of the early history of a technique that has since found widespread adoption in countless forms. Pohl recounted clear inspiration from the scanning tunneling microscope.[19] And so from its outset, SNOM has used light–matter interactions within the SPM tip–sample junction to circumvent the diffraction limit and study materials.[21]

While both SPM and SNOM measurements were initially demonstrated in ambient conditions, implementations in UHV and at cryogenic temperatures have benefited from the improved instrumental and tip-sample junction stability and so it has become possible to use light–matter interactions at the atomic-scale to study materials.[22, 23] At the same time, the combination of UHV and low temperatures also enables the observation of properties or phenomena that only occur or become detectable under these conditions.[1, 24] These include structural, electronic, and optoelectronic properties, as well as highly sensitive phonon modes, and hybrid light–matter states.[9] Importantly, the energy and spatial resolution found in these conditions permits the ability to define these phenomena with respect to atomic landscapes. In this review we primarily focus on cryogenic UHV studies of materials performed with one type of apertureless scattering-

type near-field scanning optical microscopy (s-SNOM), tip-enhanced Raman spectroscopy (TERS). Methods such as these use far-field excitation coupled into the near-field of the SPM tip along with the detection of inelastically scattered photons in the far-field, as shown for STM-TERS in **Fig. 1(a)**. To frame STM-TERS within the larger field of methods that couple light-based processes into the tip–sample junction of an SPM in cryogenic UHV conditions, we also introduce another technique that relies on the detection of visible light emitted from the tip–sample junction alongside a few recent applications. In scanning tunneling microscope induced luminescence (STML), light emission is locally stimulated by electrons tunneling inelastically within the junction of the surface and tip. These photons are then detected in the far-field as shown in **Fig. 1(b)**. For more thorough general reviews of these other techniques as well as underlying theory, we refer the interested reader to review articles that focus on these methods in each relevant section.[25] Ultimately, these methods provide new tools to study the properties of materials **(Fig. 1(c))**. While we necessarily limit this review to methods that rely on far-field detection of visible light, for completeness we mention other techniques that use alternative excitation sources or detection schemes in the conclusion, as other phenomena relevant to 2D materials occur at different time and energy scales.

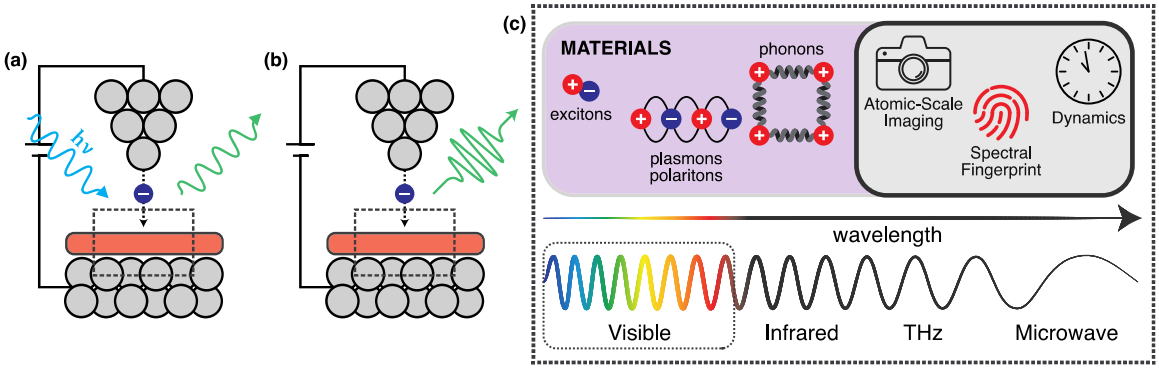

FIG. 1. Illustrations of potential light–matter interactions within an STM. (a) Far-field excitation leads to a highly enhanced near-field within the STM tip–sample junction. Scattered light is detected in the far-field. (b) Electronic tip–sample interactions within the STM result in photon emission that is detected in the far-field. (c) Various phenomena that have been investigated with the techniques on the left along with the information that can be provided.

II. Tip-enhanced Raman Spectroscopy

As previously mentioned, many of the early experiments demonstrating scattering-type near-field optical microscopy (s-SNOM) relied on light transmission through an aperture with a diameter smaller than the wavelength of light.[18, 26-31] And in fact aperture-based s-SNOM remains quite active as technological advancements drive improvements in the fabrication of the crucial probe tip.[32, 33] Light excitation and collection can both be accomplished through a nanoaperture at the apex of the otherwise metal-coated tapered optical fiber that serves as the probe.[34] While this method has been previously implemented into cryogenic UHV-SPM systems,[35, 36] here we will instead focus on apertureless methods.

The implementation of s-SNOM into a cryogenic UHV chamber can be challenging due to the required optical access to the tip–sample junction for both collection and excitation. This can potentially compromise the ability to reach and maintain low temperatures due to the necessity to introduce ports into the thermal shielding that typically surrounds the SPM head in low temperature UHV systems. Some early efforts kept the final focusing and collection optics outside of the UHV chamber so their alignments could be finely tuned easily.[37-39] However, more recently these optical elements (lenses[40-42] or a parabolic mirror[43-45]) have been moved into the UHV chamber

as close to the tip–sample junction on piezoelectric drivers to maximize their collection efficiency while still maintaining the ability to adjust their alignment. The other optical elements typical of Raman spectroscopy are necessarily kept outside of the UHV chamber, including the optical excitation source (laser) and detector (spectrometer). As a result, optical alignment requires the adjustment of both the *in vacuo* and more easily accessible optical elements. Overall, the implementation of s-SNOM into a cryogenic UHV chamber requires the careful consideration of several factors while simultaneously striking a balance between the SPM function optical excitation and detection.

Tip-enhanced Raman spectroscopy (TERS) falls within the broader category of s-SNOM, drawing clear initial inspiration from surface-enhanced Raman spectroscopy. Surface-enhanced Raman spectroscopy was initially observed in electrochemistry research in the mid to late 1970s when submonolayer coverages of molecules, such as pyridine, yielded unexpectedly strong Raman spectra on roughened silver electrode surfaces.[46-48] At the time this was attributed to two possible mechanisms, but over time the principal contribution was found to arise from an electromagnetic enhancement, where the interaction of light with particles much smaller than the incident wavelength drives the coherent oscillation of surface conduction electrons which is known as a localized surface plasmon.[49] This near field strongly enhances the Raman scattering process,[50] and has resulted in the ability to obtain optical vibrational spectra of a single molecule.[51-54]

In 1985, shortly after the demonstration of the STM and acknowledging the relatively recent discovery of surface-enhanced Raman spectroscopy, Wessel proposed surface-enhanced optical microscopy (SEOM).[55] This may be considered a reinvention of

the method proposed by Synge much earlier, and a precursor to TERS.[16] When Synge initially described his idea of near-field optical microscopy, he focused on two of the most important experimental limitations: (1) a very intense source of illumination and (2) the ability to make very small adjustments in the position of a sample, on the order of 10^{-7} cm. The widespread adoption of lasers addressed the first issue, while the invention of the STM and the ability to use piezoelectric translators to precisely raster scan a probe or sample addressed the second. In fact, when Wessel proposed SEOM, he acknowledged clear inspiration from the STM. In SEOM, a laser beam is incident on a submicrometer-sized plasmonic particle that is kept extremely close to the surface, yielding a confined and enhanced electric field. By scanning the surface across the probe particle, Wessel expected the ability to obtain excellent signal for measurements with 5 nm spatial resolution based on the confinement of light in the near field.[55] Over time, the spatial resolution of TERS measurements would improve to provide subnanoscale spatial resolution through improvements to the instrumentation and technique, as well as implementation into cryogenic UHV conditions. While the first UHV-TERS studies focused on thin films or submonolayer coverages of organic molecules on a surface,[37, 56, 57] the ubiquitous use of Raman spectroscopy to characterize low-dimensional materials,[58, 59] along with the ability to fabricate new materials in UHV, quickly led to efforts to develop instrumentation capable of cryogenic UHV-TERS. These works will now become our focus, while a broader review of TERS studies of 2D materials performed in ambient conditions is available elsewhere.[60]

In one of the first demonstrations of UHV-TERS of a low-dimensional material, Shiotari, Kumagai, and Wolf investigated graphene nanoribbons (GNRs) on a Au(111)

substrate at room temperature.[61] They used an on-surface polymerization technique to fabricate GNRs on the surface beginning from halogenated aryl precursor molecules via an Ullmann-like coupling reaction, shown in **Fig. 2(a)**, that has been extensively used to fabricate carbon nanostructures on surfaces.[62-65] Thermal annealing resulted in the formation of 7-armchair graphene nanoribbons (7-AGNRs),[66, 67] which were first visualized with STM imaging shown in **Fig. 2(b)**. By positioning the tip over a 7-AGNR, they were able to obtain strongly enhanced near-field Raman spectra that exhibited the radial breathing-like phonon mode (RBLM), D band, and G band characteristic of GNRs as shown in **Fig. 2(c)** in the spectrum labeled **(iii)**. Notably, TERS spectra acquired of the clean Au(111) surface **(i)** and polyanthrylene/Au(111) **(ii)** lacked any characteristic spectral peaks. Additionally, they noticed strong intensity fluctuations or blinking behavior when they acquired a time series of near-field spectra as shown in **Fig. 2(d)**. They attributed this blinking to thermally- and laser-induced fluctuations in the tip apex geometry by comparing the experimentally derived intensity distribution with theoretical models. Ultimately, although they were able to capture near-field Raman spectra of the 7-AGNRs, the seemingly unstable tip–sample junction prevented defining the spatial resolution more stringently.

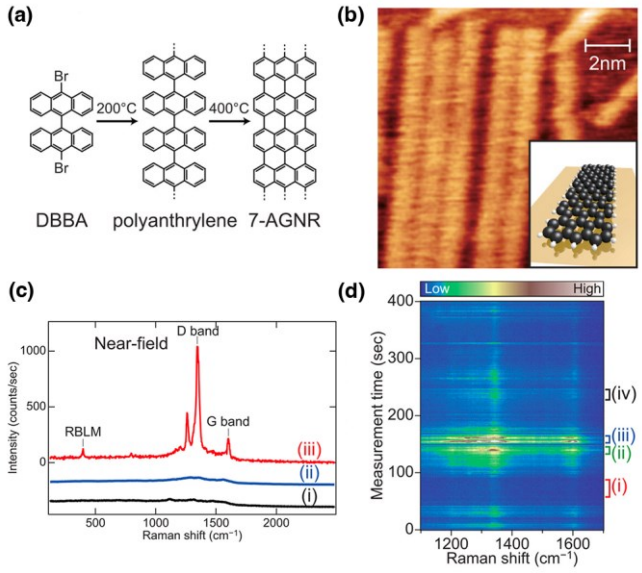

FIG. 2. STM and TERS measurements of GNRs acquired at room temperature. (a) Fabrication scheme of 7-armchair graphene nanoribbons (7-AGNRs) from 10,10′-dibromo-9,9′-bianthryl (DBBA) molecules. (b) STM image of Au(111) ∼500 °C after DBBA deposition. Inset shows a schematic illustration of the molecular structure for 7-AGNRs. (c) Near-field Raman spectra of (i) clean Au(111), (ii) polyanthrylene/Au(111), and (iii) 7-AGNR/Au(111). The spectra were measured over 1 s with the tunneling conditions of (i) and (iii) $V_s = -0.05$ V and $I_t = 1$ nA and (ii) $V_s = -0.5$ V and $I_t = 0.1$ nA. $\lambda = 632.8$ nm. The spectra for (i) and (ii) are vertically shifted for clarity. Time evolution of TERS spectra for 7-AGNR/Au(111). Each spectrum was obtained every 1 s with the tunneling conditions of $V_s = -0.05$ V and $I_t = 1$ nA. Reprinted (adapted) with permission from Ref. [61]. Copyright 2014 American Chemical Society.

Even though the previously mentioned study was performed in UHV, benefiting from the pristine environment and well-defined sample, the tip–sample junction was found to exhibit significant instability. By cooling the system down to cryogenic temperatures, it becomes possible to significantly improve the mechanical stability of both the tip and sample, as well as minimize thermal drift and improve the energy resolution of spectra. This has led to unprecedented spatial resolution, approaching the atomic-scale, as well as the ability to identify subtle effects.[41, 68-71] This includes the

ability to probe phonon modes near the atomic-scale to identify highly localized strain within heterostructures,[72] define atom-resolved images of ionic lattices,[73] and image single atomic adsorbates[74] among others.[75] Furthermore, the improved stability leads to the ability to perform longer duration measurements, such as TERS mapping or line scan experiments, which provide the means to generate real-space spectroscopic images and estimate the lateral resolution of the enhanced near field. While TERS mapping and line scan measurements have been extensively used for nanoscale studies of materials in ambient and room temperature conditions,[76-79] the spatial resolution has been found to substantially improve at cryogenic temperatures in UHV.[80] By acquiring sequential TERS spectra with the tip positioned according to a defined pattern, such as at discrete points in a grid or line, a full Raman spectrum is acquired at each pixel. This essentially enables hyperspectral imaging, where the evolution of specific vibrational modes can be tracked in real-space with a TERS map or line scan.[81] Importantly, the acquisition of TERS maps or line scans can take significant amounts of time, even a few or tens of seconds per pixel or point. As a result, the mechanical stability found at low temperatures in UHV becomes critical to achieve the highest degree of spatial resolution. These methods have come to represent an essential aspect within TERS measurements and have led to the realization that the supreme stability of the tip–sample junction enables new approaches that demonstrate subnanoscale spatial resolution.

Within this context, recent TERS studies have focused on low-dimensional allotropes of carbon group elements that can be fabricated *in vacuo* on a supporting substrate. Specifically, graphene analogues composed of silicon or boron have been investigated. In 2012, silicene, a 2D honeycomb lattice of silicon was first fabricated on a

Ag(111) surface and studied with STM.[82] Following this work, silicene was studied with far-field Raman spectroscopy with both experimental and theoretical approaches.[83-86] However, from the beginning STM imaging revealed the presence of complex and diverse phases within silicene, therefore requiring spectroscopic characterization with a high degree of spatial resolution. In 2017, silicene on Ag(111) was investigated with UHV-STM-TERS performed at 77 K.[87] The multiple phases, T and $\sqrt{13} \times \sqrt{13}$ phases, observed in STM images, shown in **Fig. 3(a)**, could be spectroscopically identified based on characteristic TERS spectra, shown in **Fig. 3(b)**, acquired with the tip positioned over each phase. Furthermore, defects, edges, and even local strain between domain boundaries **(Fig. 3(c))** were identified based on the phonon modes observed in TERS spectra **(Fig. 3(d))** with a reported enhancement factor as high as 10^9, compared to far-field Raman spectra acquired with the tip retracted from the surface, and 0.5 nm spatial resolution. While silicon atoms form a 2D honeycomb lattice on Ag(111), silicon atoms have been found to form unstable clusters or nanoribbons on the anisotropic Ag(110) surface.[88, 89] However, the arrangement of atoms within these structures could only be poorly defined with STM requiring spectroscopic methods that lacked spatial resolution.[90, 91] With the high spatial resolution of TERS, Sheng *et al.* acquired vibrational fingerprints of Si clusters and single-strand nanoribbons (SNRs) directly supplementing STM images with spectroscopy. Based on the phonon modes observed in TERS spectra of a nanocluster **(Fig. 3(e))**, with a spatial resolution near STM, they defined a pentagonal atomic structure as shown in the inset of **Fig. 3(f)**. Furthermore, they found that the observed TERS intensity of specific phonon modes of single-strand silicon nanoribbons **(Fig. 3(g))** are sensitive to the tip–sample distance as maintained by

manipulating the feedback parameters of the STM, in this case the setpoint tunneling current **(Fig. 3(h))**.

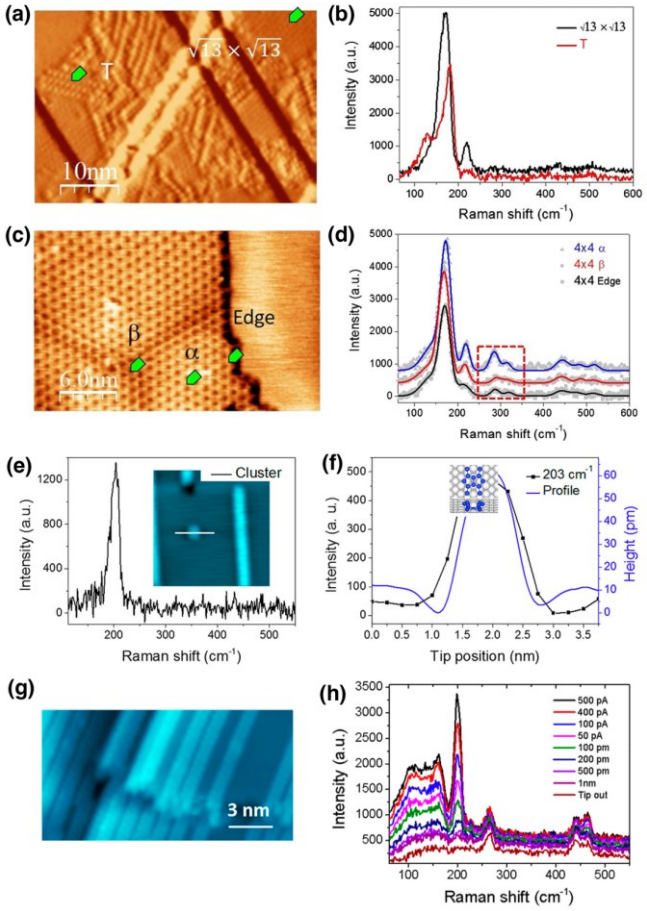

FIG. 3. STM and TERS measurements of silicene on Ag(111) and silicon nanostructures on Ag(110). (a) STM topography of coexisting silicene T phase and $\sqrt{13} \times \sqrt{13}$ phase. (b) TERS spectra of the T phase and well-ordered $\sqrt{13} \times \sqrt{13}$ phase, with the tip at the corresponding position marked in (a) (1 V, 100 pA), shows very different spectra. (c) STM topography of silicene $4 \times 4 - \alpha$ phase and β phase. (d) TERS spectra of the $4 \times 4 - \alpha$ phase, β phase, and domain edge, with the tip at the corresponding positions in (c) (1 V, 50 pA). The far-field signal has been subtracted from all the TERS spectra, the acquisition time is 50 s, $\lambda = 532$ nm, and the laser power is about 10 mW. Figure and caption reprinted with permission from Ref. [87]. Copyright 2017 by the American Physical Society. (e) TERS spectrum of the Si cluster in the inset STM image. (f) TERS intensity

profile of the $203\ \mathrm{cm}^{-1}$ mode along the line in (e) with an interval of 0.25 nm every step, and the STM topography height profile (blue line). (g) STM images of SNRs grown at room temperature. (h) Gap-distance dependent TERS spectra of SNRs (1 V). $\lambda = 532\ \mathrm{nm}$. Reprinted (adapted) with permission from Ref. [92]. Copyright 2014 American Chemical Society.

Following their study of silicene, the same group used TERS to study the vibrational properties of borophene,[93] a relatively recently discovered 2D allotrope of boron that can be fabricated on supporting metal substrates.[94-96] The complicated chemistry of boron observed in the bulk material was found to have similar effects in 2D structures, resulting in polymorphic diversity in the mono-elemental system. Boron atoms form highly delocalized bonds by sharing electron pairs among three or more atoms.[97] This results in remarkable chemical and mechanical properties including extremely high bending flexibility and in-plane elasticity.[98, 99] When fabricated on a Ag(111) surface, borophene has been found to form two distinct phases that can be defined by a triangular lattice with different densities of periodic hole arrays.[100] The STM image shown in **Fig. 4(a)** and the atomic lattice shown in **Fig. 4(b)** illustrate what is referred to as β_{12} or $\nu_{1/6}$ borophene.[93] As shown in **Fig. 4(c)**, Sheng *et al.* acquired TERS spectra of β_{12} borophene that showed a strongly enhanced peak at $189\ \mathrm{cm}^{-1}$ that corresponds to the B_{3g}^2 phonon mode that consists of nearly entirely vertical atomic displacements. They found they were able to spectroscopically identify the phase of a borophene sheet with 1 nm spatial resolution.

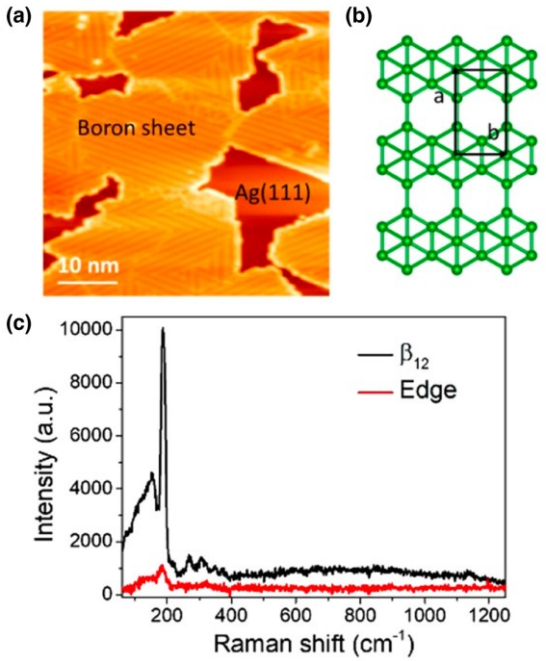

FIG. 4. STM and TERS measurements of borophene on Ag(111). STM topography of a β_{12} borophene sheet on a Ag(111) surface (3.9 V, 270 pA). (b) Schematic atomic structure model of β_{12} borophene with a rectangular unit cell of $a = 0.5$ nm, $b = 0.3$ nm. (c) TERS spectra with the tip on the terrace and at the edge of a borophene island showing the strongly enhanced B_{3g}^2 mode (0.3 V, 100 pA, 10 s). $\lambda = 532$ nm. Figure and caption reprinted (adapted) with permission from Ref. [93]. Copyright 2019 American Chemical Society.

When integrated into van der Waals heterostructures, the lattice mismatch between materials can result in localized strain that strongly affects mechanical, optical, and electronic properties.[101, 102] In ambient conditions, TERS has been used to study highly localized strain in graphene,[103] MoS_2/Au heterostructures,[104] and nanostructures[105, 106] among others.[107] Based on the expected mechanical properties of borophene, efforts have been made to integrate it as a supporting substrate in a vertical heterostructure to realize its potential within devices. Instead of vertical heterostructures, these early works found that borophene formed abrupt lateral heterojunctions with organic molecules,[108]

graphene,[109] or graphene nanoribbons.[110] These observations were attributed to preferential adsorption of the secondary species onto the supporting Ag(111) substrate instead of borophene. To address this and probe the effects of molecular adsorption on the lattice of borophene, Li *et al.* deposited a monolayer of tetraphenyldibenzoperiflanthene (DBP) onto a Ag(111) surface that was already covered by borophene. They found that in this case, DBP would adsorb onto the borophene and considered this mixed vertical heterostructure with STM and TERS as shown in **Fig. 5(a)**. As previously mentioned, borophene can form two distinct phases on the Ag(111) phases, which can be differentiated based on characteristic phonon modes. Despite being covered by DBP, the authors identified these phases with TERS mapping of these specific vibrational modes that were found to shift due to molecular adsorption as demonstrated in **Fig. 5(b)**. However, beyond the simple identification of buried borophene phases, by comparing experimentally acquired TERS spectra with simulations **(Fig. 5(c))**, they were able to identify that molecular adsorption induced ~0.6 % tensile strain **(Fig. 5(d))** within the atomic lattice of underlying borophene. Furthermore, by deliberately using the STM tip to remove individual molecules they found that the molecule-induced strain could be reversibly released as confirmed with TERS line scan measurements that demonstrated angstrom-scale spatial resolution as shown in **Fig. 5(e,f)**. The high spatial resolution also revealed a delicate strain spillover effect propagated within the borophene lattice ~1 nm beyond the location of molecular adsorption.

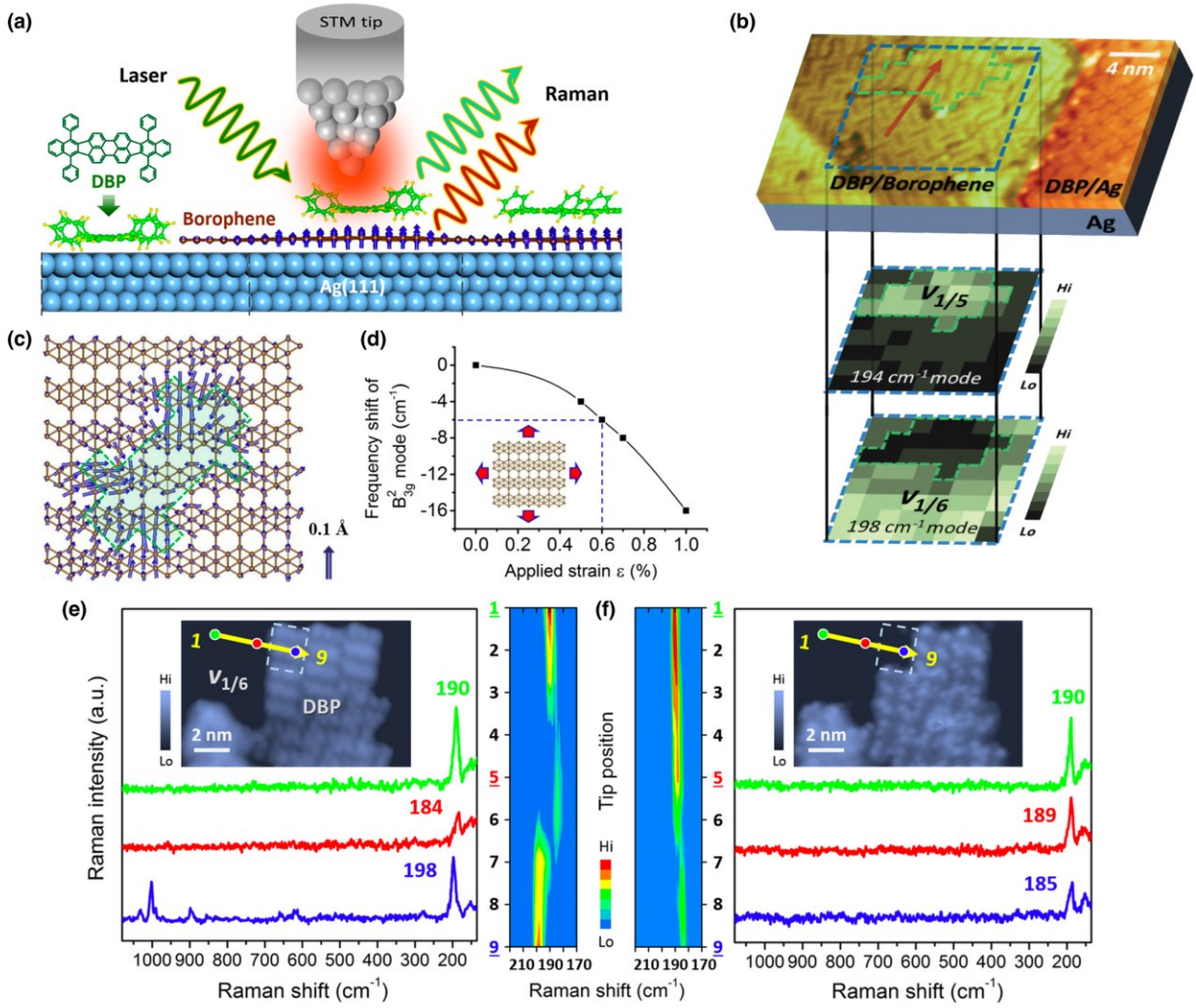

FIG. 5. STM and TERS characterizations of local strain in DBP/borophene vertical heterostructures. (a) Experimental schematic including the molecular structure of DBP. The blue arrows denote boron atomic displacements in the borophene monolayer. (b) (top) STM image (2 V, 500 pA) of sub-monolayer mixed-phase borophene covered by a DBP layer. The molecular domains supported on borophene are shaded in yellow-green for clarity. The blue square marks the scanned region for 2D TERS mapping, with a green polygon indicating the domain boundary. (bottom) TERS intensity maps (0.5 V, 500 pA, 8 s, 8 pixels × 8 pixels) of the 194 cm^{-1} and 198 cm^{-1} modes over the region marked with the blue square in the STM image above. (c) Top view of the adsorption configuration for DBP on $v_{1/6}$ borophene with blue arrows to denote boron atomic displacement. The green contour indicates the position of the DBP molecule. (d)

Correlation between the frequency shift of the B_{3g}^2 mode and the lattice strain of $\nu_{1/6}$ borophene. Inset: corresponding theoretical model involving biaxial tensile strain applied to the borophene lattice. (e,f) Spectral evolution of 1D TERS measurements (0.5 V, 500 pA, 10 s per point, 9 points, $\lambda = 561$ nm) along the yellow-line trace displayed in the inset STM images. Both before (e) and after (f), the removal of two DBP molecules from the top of the borophene. Figure and caption reprinted (adapted) with permission from Ref. [72]. Copyright 2021 American Chemical Society.

At cryogenic temperatures it becomes possible to reliably manipulate atoms or molecules within the tip–sample junction.[111, 112] While the previously mentioned study removed molecules with the STM tip to prove the origin of strain within an underlying substrate as shown in **Fig. 5(e,f)**, it is also possible to deliberate absorb a molecule or atom onto the apex of the tip, therefore functionalizing the tip. This enables the ability to use interactions between the functionalized tip apex and the surface to probe the properties, such as the atomic structure and electrostatic potential, of a material in unique ways.[113-117] In this manner, Crampton *et al.* used a cobalt tetraphenylporphyrin (CoTPP)-terminated silver tip to achieve atomically resolved ion selective imaging of an insulating Cu_2N monolayer fabricated on a Cu(100) surface.[73] **Fig. 6(a)** shows the correlation between TERS spectra for a CoTPP adsorbed onto the Ag tip and a CoTPP molecule lying on the Cu(100) surface. Then, with the CoTPP-functionalized tip they found that by tracking the TERS intensity of the $1568\ \mathrm{cm}^{-1}$ mode they could image the atomic lattice of a monolayer of the ionic insulator, Cu_2N as can be seen in **Fig. 6(b)**. In comparison with STM imaging **(Fig. 6(c))**, they found that the spatial resolution of TERS imaging matched the resolution found in the STM topography as represented in the extracted line scans in **Fig. 6(d)**. Bias-dependent STM imaging was used to confirm the location of N atoms within the lattice (**Fig. 6(e,f)**). Furthermore, they asserted that by tracking the

spectral shift of specific vibrational modes, they could define ion selective images based on Stark shift maps. While in this case, they used an aromatic polyatomic molecule to probe the surface, they have also reported similar studies of molecular systems with a tip functionalized with a single CO molecule.[115-117] The use of a probe molecule enables the study of electronic and structural properties through mapping electrostatic forces that may not otherwise be observable with Raman spectroscopy.[118, 119]

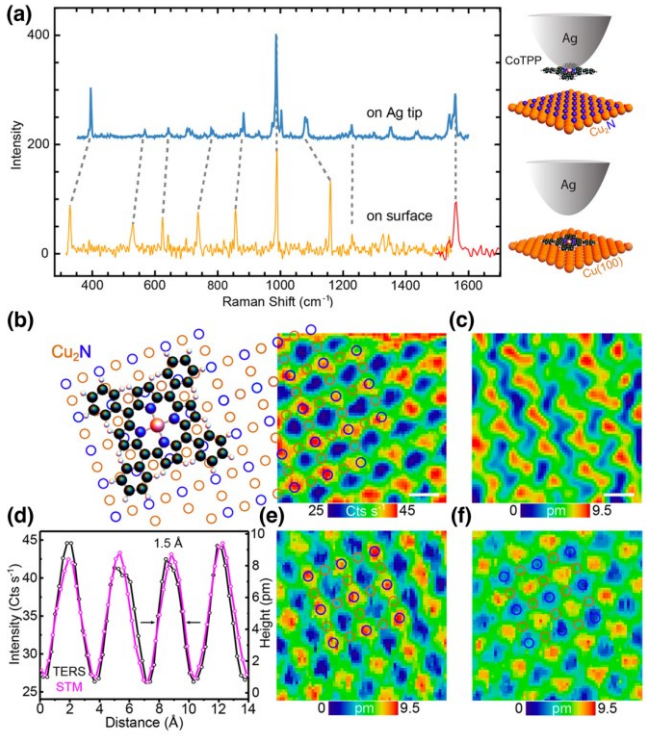

FIG. 6. STM and TERS imaging of Cu_2N with a molecule-terminated silver tip. (a) Correlation between TERS spectra of tip-attached cobalt tetraphenylporphyrin (CoTPP) and CoTPP adsorbed on Cu(100) with the tip placed on the central Co atom. Corresponding models of the systems appear on the right. $\lambda = 634$ nm. (b,c) simultaneously recorded TERS line intensity of the $1568\ \mathrm{cm}^{-1}$ mode and STM topography (set point 1 nA, 15.5 mV). The schematic extension of the TERS image in (a) is made to clarify the atomic resolution, which is unrelated to the footprint of the molecule. (d) Line cuts taken from the STM topographic image at –1 V (e) and TERS image (b). The N sites appear as protrusions in the STM and TERS images with

comparable spatial resolution of ~1.5 Å full width at half maximum. (e,f) Contrast inversion of STM topography acquired at –1 V (e) and +1 V (f), respectively (set point 0.1 nA). Images are low-pass filtered for clarity. Figure and caption reprinted (adapted) with permission from Ref. [73]. Copyright 2019 American Chemical Society.

The most recent studies of molecules with TERS that have demonstrated intramolecular spatial resolution have relied on increasingly small tip–sample gap distances. Over time, experiments and theory have come to suggest that the spatial resolution of TERS measurements approaches the angstrom-scale when light is confined to the atomistic near-field and the tip–sample gap distance becomes typically < 2 Å.[70, 120, 121] Importantly, this approach necessitates the supremely stable conditions found in UHV and low temperatures, as otherwise the tip–sample junction becomes unstable. Following their characterization of the electronic structure of ultrathin ZnO layers epitaxially grown on a Ag(111) surface with TERS,[44] Liu, Wolf, Kumagai, and co-workers investigated TERS spectra of a material where the tip–sample gap vanishes and atomic point contact (APC) is made.[122] They first considered ultrathin layers of ZnO on Ag(111) as shown in the STM image in **Fig 7(a)**. TERS spectra acquired with the tip positioned over 2-monolayer (ML) ZnO at different tip–sample gap distances revealed that spectra change significantly in the vicinity of the APC. They attributed this to a combination of electromagnetic and chemical enhancement (via electronic resonance) based on their previous characterization of the electronic structure of the ZnO layers. Additionally, they found that the APC could be formed and broken in a reversible manner as illustrated in the waterfall plot of TERS spectra shown in **Fig. 7(b)**, where the spectral evolution about the APC regime was observed to be symmetric. They specifically considered the vibrational mode at 395 cm^{-1} that was defined to be the result of contact between the tip

and ZnO and was identified specifically as a local out-of-plane stretching mode of an oxygen atom in the second layer based on density functional theory calculations as illustrated in the model in **Fig 7(d)**. The authors suggested that interactions between the Ag tip and oxygen atoms in the first layer resulted in charge rearrangement and led to stiffening in the interlayer bond within ZnO therefore resulting in the observed $395\ \mathrm{cm}^{-1}$ mode. Furthermore, they attributed the dramatic enhancement of TERS intensity upon APC formation to hybridization between the tip and sample, mentioning that this approach could increase the sensitivity and capability of TERS to consider other materials.

Most TERS studies rely on a plasmonic supporting substrate in addition to the plasmonic probe, i.e., silver tips are used with silver substrates. This results in the so-called gap mode configuration where plasmonic modes couple between the tip and substrate and tunnel across the junction.[123, 124] Based on their observation of a significant increase in TERS intensity when the tip is brought into contact with a sample, Liu, Wolf, Kumagai, and co-workers used a similar method to study the phonons of the Si(111)-7 × 7 surface.[125] They first visualized the surface with STM while illuminated with the 633 nm laser that they also used as the source for TERS measurements. As can be seen in **Fig. 7(e)**, illumination during scanning led to the formation of atomic defects that occur only in faulted half unit cells. And so, they used STM imaging to identify unfaulted half unit cells where they brought the Ag tip into atomic point contact with the surface and recorded TERS spectra, **Fig. 7(f)**. Aside from the constant observation of the optical phonon mode of bulk Si at $520\ \mathrm{cm}^{-1}$, they noted the emergence of characteristic Raman peaks that they assigned to surface phonons within the APC regime. Based on

this, they suggested that, in principle, APC could be used to study other nonplasmonic substrates and understand light–matter interactions at the atomic-scale in metal–semiconductor heterostructures.

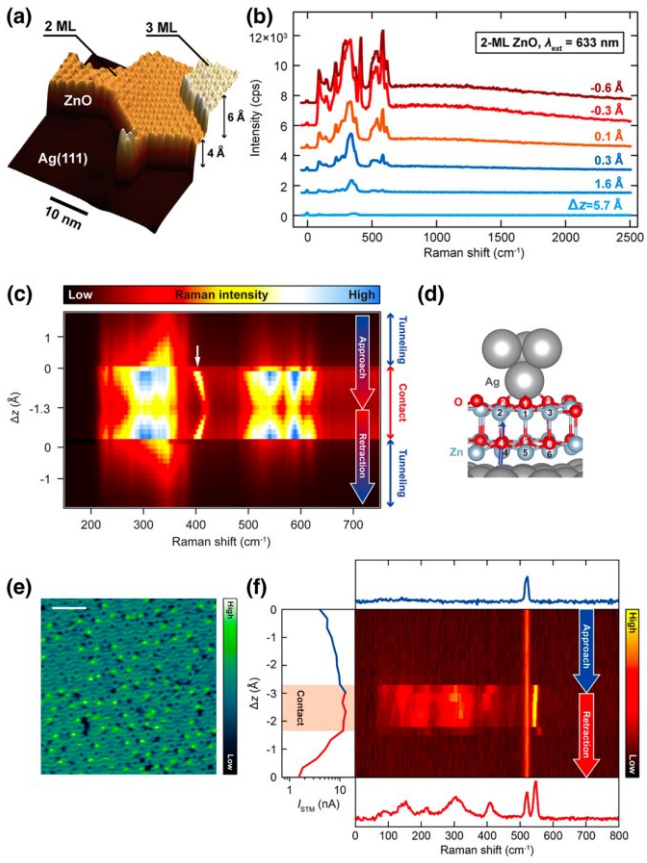

FIG. 7. STM and atomic point contact (APC) TERS of materials. (a) Quasi 3D STM image of ultrathin ZnO layers epitaxially grown on the Ag(111) surface (V_{bias} = 1 V, I_t = 100 pA). (b) TERS spectra of 2-ML ZnO recorded at different tip-sample gap distances as indicated in the figure (Ag tip, $\lambda = 633$, $F = 0.29\ mW\ \mu m^{-2}$, t_{acq} = 3 s per spectrum, T = 10 K). (c) Waterfall plot of the gap-distance-dependent TERS spectra recorded over 2-ML ZnO (Ag tip, $\lambda = 633$, $F = 0.36\ mW\ \mu m^{-2}$, t_{acq} = 300 s per spectrum, T = 10 K). The tip approaches and retracts toward and backward from the ZnO from the tunneling to the APC regime. (d) Optimized structure with the Ag tip. The characteristic vibrational mode resulting from the quantum point contact is shown by the blue arrow. Figure and caption reprinted (adapted) under a Creative Commons Attribution (CC BY) License from Ref. [122]. Copyright 2020 American Chemical Society.

(e) STM image of Si(111)-7 × 7 under illumination (T = 10 K, V_{bias} = 0.3 V, I_t = 1 nA, P_{ext} = 0.7 W/cm^2, scale bar = 5 nm, $\lambda = 633$). (f) Waterfall plot of TERS recorded during tip-approach and retraction over Si(111)-7 × 7 (10 K, V_{bias} = 0 V, $\lambda = 633$, P_{ext} = 0.7 mW/μm^2). The left panel shows the simultaneously recorded $I_{STM} - \Delta z$ curve. Although the V_{bias} is nominally set to zero, the current occurs due to the photovoltage under illumination. The red shaded region indicates the APC. The top and bottom panels display the TERS spectra in the tunneling and contact regimes, respectively. Figure and caption reprinted (adapted) under a Creative Commons Attribution (CC BY) License from Ref. [125]. Copyright 2021 American Chemical Society.

The continuing realization of new 2D materials as well as increasing efforts to fabricate heterostructures composed of disparate materials requires the ongoing development of new characterization methods. The previously discussed TERS studies of low-dimensional materials have demonstrated the ability to use near-field Raman spectroscopy to probe and define phonon modes that can be used to identify phases, as well as highly localized phenomena. This includes defects and even interactions between layers that may manifest in the form of lattice strain. Since many TERS studies focus on molecular systems, perhaps due to lasting influences from its inspiration from surface-enhanced Raman spectroscopy, its application to studies of materials remains comparatively unexplored. The studies mentioned here demonstrate the powerful potential of this technique to characterize phonons of materials with angstrom-scale spatial resolution.

III. Scanning tunneling microscope induced luminescence

In a manner that predates scanning tunneling microscope induced luminescence (STML), but is conceptually similar, Young, Ward, and Scire used a field emission probe

brought close to a conducting surface in 1972 and measured secondary electron emission with an electron multiplier detector pointed towards the sample surface.[126, 127] In this manner, they were able to generate topographic maps of a 180 line/mm diffraction grating with 30 Å vertical and 4000 Å lateral resolution with an instrument that they coined the Topografiner. Later, based upon observations of photon emission from metal-oxide-metal tunnel junctions[128] and surfaces exposed to low-energy electron beams[129] through what was attributed to inelastic electron tunneling (IET) processes, Gimzewski *et al.* placed a photon detector near the tip–sample junction of an STM in 1988.[130] They observed light emission from the tunneling gap of a STM. Since the tip becomes the source of excitation in STML the instrumental setup becomes relatively simpler compared to apertureless s-SNOM. The optical elements within the UHV chamber are only used for the collection of emitted photons that are generated by tunneling electrons, resulting in the use of optical elements with high numerical apertures, such as parabolic mirrors or a single lens that is as large and close to the tip–sample junction as possible.[131, 132] Perhaps due to the fact that the STM tip becomes the excitation source and no external source is required, recent advances in STML measurements have focused on the development of new detection methods, moving beyond a spectrometer to attain unprecedented time resolution of dynamic processes that will be discussed later. STML has become an extremely powerful method to probe a material at the atomic scale since the light generated within the STM junction carries information that describes the structure under investigation.

Initial demonstrations of STML attributed the light emission to one of two possible mechanisms resulting in a technique capable of studying optical and electronic

properties of molecules and materials. Light emission from the tip–sample junction was proposed to arise from inelastic electron tunneling processes or the injection of hot electrons.[133] This provides the ability to use STML to measure multiple types of phenomena such as overbias emission,[134] photon pair emission,[135] and electron–hole recombination that leads to excitation emission.[136] Importantly, the observation of light emission from recombination processes requires that the emitter be decoupled from a metallic substrate. In the case of molecular systems, this has been accomplished by the growth of multilayers of molecules or thin insulating layers, such as Al_2O_3 or NaCl,[15, 136-138] with studies even reporting the ability to resolve vibronic features that correspond to a Raman vibrational fingerprint.[139, 140] Some early STML studies of materials used noble metal substrates[141, 142] demonstrating atomic resolution in STM-induced photon emission images of the Au(110) surface.[143] More recently, STML has been used to study engineered materials, such as several-atom long silver chains on the NiAl(110) surface[144] and thin films of oxides on gold substrates.[145-147] Here we highlight a few recent studies that used unique methods to probe materials with STML.

Aside from insulating layers, the STM tip itself can also be used to decouple a material from the substrate enabling the observation of its optoelectronic properties. As shown in **Fig. 8(a)**, Chong *et al.* used the STM to lift one end of an individual GNR from a Au(111) surface,[148] forming a GNR junction in a manner that has previously been used to study the conductance of a single GNR.[149] By placing the STM tip over the terminus of a GNR and ramping the bias voltage they were able to dehydrogenate a terminal carbon, where H-terminated **(Fig. 8(b))** and C-terminated **(Fig. 8(c))** species have distinct appearances in STM imaging. Furthermore, the decay of the conductance while the tip

was retracted was used to verify the formation of a GNR junction, based on the decreased decay rate for retraction compared to the approach as shown in **Fig. 8(d)**. They found that STML spectra of H-terminated GNRs yielded weak featureless emission spectra, while spectra of C-terminated GNRs exhibited sharp features suggestive of a radiative transition intrinsic to the GNR **(Fig. 8(e))**. Furthermore, the spectra were found to exhibit both applied voltage **(Fig. 8(f))** and tip–sample gap distance **(Fig. 8(g))** dependence. In this manner, they were able to reveal new insight into the optical transitions of GNRs by considering a single GNR bridging the gap between the gold coated tungsten tip and Au(111) substrate.

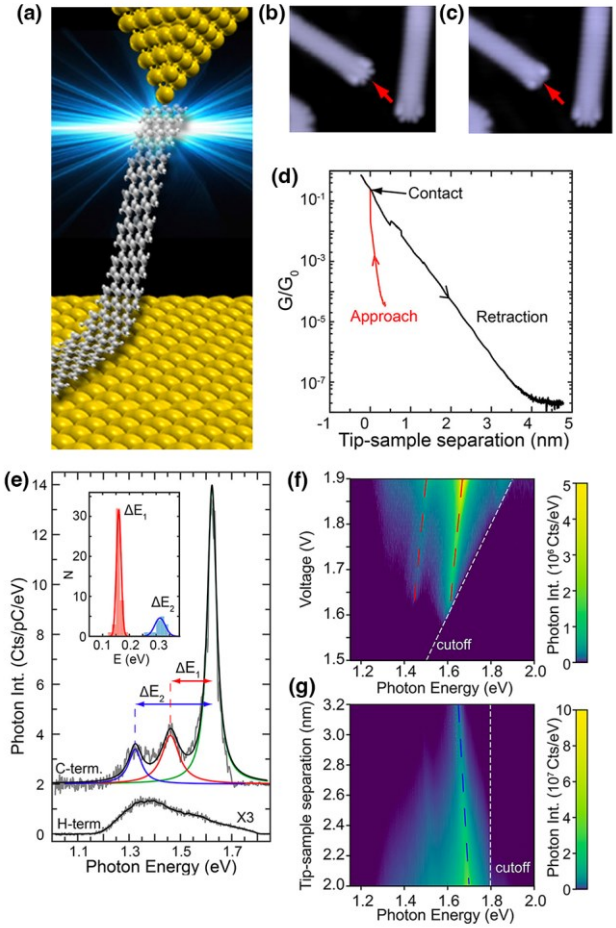

FIG. 8. Electroluminescence from a single graphene nanoribbon in the STM tip–sample junction. (a) Schematic of the experimental configuration. (b) STM image of H-terminated 7-armchair GNRs on Au(111) (0.5 $nm^2 \times 7.4\ nm^2$, V = 0.05 V, I = 0.1 nA). (c) STM image of the same area after dehydrogenation of the central carbon atom of the ribbon terminus marked by an arrow. (d) Normalized conductance G/G_0 versus tip–sample distance z for a 7-AGNR, in the position marked by an arrow in (b) (V = 0.1 V). (e) STML spectra of the suspended ribbon when H-terminated (bottom curve, magnified by a factor 3, z = 3.2 nm, V = 1.8 V, I = 14.8 nA, acquisition time t = 60 s) and when C-terminated (top curve, vertically shifted, z = 3.2 nm, V = 1.7 V, I = 0.4 nA, t = 60 s). The inset shows the distribution of the energy shifts of the two low-intensity features from the main peak, that is ΔE_1 and ΔE_2, obtained from measurement with different C-terminated junctions. (f,g) Voltage (z = 3.2 nm) and tip–sample distance (V = 1.8 V) dependencies of the STML spectra, respectively. Figure and caption reprinted (adapted) with permission from Ref. [148]. Copyright 2018 American Chemical Society.

The atomic resolution of STML makes it an ideal method to study photon emission that arises from individual atomic defects. Schuler *et al.*, grew WS_2 islands on epitaxial graphene supported on a SiC substrate and considered atomic defects within the top layer of WS_2 with a combination of SPM methods and STML.[150] They found that inelastic electron tunneling from the gold-coated tip into single sulfur top vacancies led to photon emission. Emission was found to be highly localized and dependent upon the location of charge injection by the STM tip as can be seen in the STML image. Furthermore, the defect also exhibited photon emission at a tunneling bias significantly lower than the surrounding pristine WS_2. They supplemented these spectral measurements with high-resolution SPM imaging. Ultimately, with a focus on the high spatial resolution, they were able to characterize individual atomic defects within the 2D semiconductors, therefore realizing atomic-scale single-photon sources.

Fluctuations induced within the well-controlled atomic-scale environment observed in a low temperature UHV-STM can be used to probe the effects of atomic-scale processes on light emission from a picocavity. Rosławska *et al.* used STML to develop an understanding of how the plasmonic properties of the tip–sample junction change at the single-atom limit.[151] As shown in **Fig. 9(a)**, while recording an STM image of the Au(111) surface with a gold STM tip at T = 4 K, they interrupted scanning and deliberately deposited a single atom onto the surface. By simultaneously recording light emission they observed that the deposition of an atom from the gold tip significantly changed the observed photon yield **(Fig. 9(b))**. The overall electroluminescence was found to reduce due to this change in the atomic apex of the tip, with a notably reduced intensity observed when the tip was positioned on top of the deposited atom and a surface defect. Significantly, even though the atomic apex of the tip was modified, the shape of the spectral features found with STML was unchanged aside from an overall reduction in intensity **(Fig. 9(c))**. Beyond capturing the effects of the deposition of a single atom on STML spectra, the authors also considered dynamic changes when the tip was in atomic point contact with the Au(111) surface as shown in **Fig. 9(d)**. They observed that the optical spectra and integrated light intensity both undergo changes as a function of time **(Fig. 9(e,f))**, with the feedback loop of the STM causing the emission to return to its relative original intensity. They attributed these spectral fluctuations to current changes as well as mechanical stress and thermal effects that cause changes and modifications to the atomic structure of the tip. However, while the intensity was found to change significantly over the course of their measurements, they found that the shape of STML spectra remained relatively unchanged. This suggests that in addition to spectral features,

the overall intensity of an STML spectrum can be used to define the tip–sample junction. Based on their observations, they stressed the importance of atomic-scale features in the STM tip–sample junction in terms of near-field optical microscopy measurements that rely on the formation of a picocavity.[152, 153] They specifically note that in their case, even at slightly elevated temperatures, i.e., ~50 K compared to 4 K, spontaneous atomic rearrangements become probable preventing the desired observation of atomic-scale light emission.

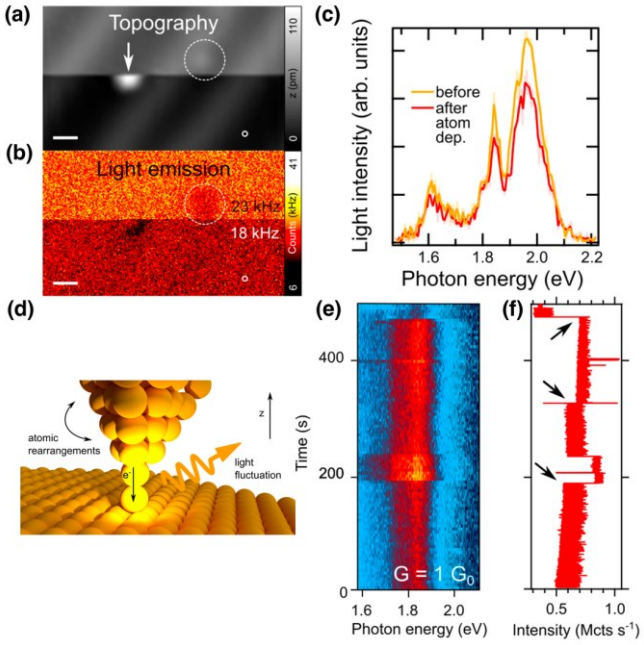

FIG. 9. STML study illustrating atomic-scale structural fluctuations. (a) STM topographic image of the Au(111) surface recorded under electron tunneling conditions, $U = -2.5$ V, $I = 1$ nA. During the scan (from top to bottom), a single atom was deliberately deposited from the tip apex onto the surface by atomic manipulation at the position marked by the arrow. Scale bar: 1 nm. (b) Light intensity map recorded simultaneously with (a). The values in the bottom and upper part of the image indicate the average light intensity before and after tip modification. (c) Optical spectra recorded on the position marked by the small circles at the bottom right of (a) and (b) before (yellow curve) and after (red curve) atom deposition; $U = -2.5$ V, $I = 1$ nA, integration time: 50 s. (d)

Illustration of the experiment in which the tip of an STM forms a single-gold-atom contact. (e) Time-trace of optical overbias emission spectra measured for a single-atom contact. The plot consists of 100 spectra, each recorded with 5 s of integration time. (f) Simultaneously recorded light intensity measured by the photon detector with a 20 ms integration time per point. The current feedback was enabled during the measurement. Figure and caption reprinted (adapted) under a Creative Commons Attribution (CC BY) License from Ref. [151]. Copyright 2021 American Chemical Society.

More recently, STML has been used to capture dynamic processes, with reviews of recent progress available elsewhere.[23, 154] Time-resolved detection of single photons has been used to probe excitation and relaxation dynamics within the STM tip–sample junction.[155, 156] Time resolved measurements have permitted the differentiation of emission mechanisms due to their different dynamics. Specifically, the excitonic and plasmonic components of emission were characterized, separated, and tuned in thin films of C_{60} supported on noble metal substrates.[157] Furthermore, the exciton[158] or plasmonic[159] dynamics of single-photon emitters within these molecular films have been probed by the combination of STM with a Hanbury Brown and Twiss interferometer. The same detection method has also recently been used to observe photon superbunching from a STM junction consisting of a Ag tip and Ag(111) substrate through a process that was found to be electrically driven.[135] Since STML relies on the STM tip to serve as the excitation source, some instrumental efforts have been focused on the development of new methods to detect the emitted photons. The ability to detect single photons with exceptional time resolution offers the potential to study dynamic processes in materials at the atomic scale.

IV. SUMMARY AND OUTLOOK

From its initial demonstrations in its various forms, near-field scanning optical microscopy has offered unique insight into materials by probing the interactions of light and matter below the diffraction limit.[160] The combination of optical spectroscopy with a scanning probe microscope provides a highly useful tool to investigate the properties of a material within the probe–sample interaction volume. Recently, atomic-scale features at the apex of the probe have become considered essential to achieving the highest degree of spatial resolution. As a result, the technique has benefited significantly from the stability found by implementations in ultrahigh vacuum (UHV) and further with low-temperature measurements. In this review, we discussed the development and recent studies of materials with two methods that rely on the detection of visible light that describes the material in the atomic-scale tip–sample junction of a cryogenic UHV scanning tunneling microscope (STM). The insight from methods such as these is expected to inform design principles for engineering materials with a focus on atomic-scale phenomena.[161]

Tip-enhanced Raman spectroscopy (TERS) relies on the highly enhanced and localized electric field generated at a plasmonic tip apex under light illumination to measure Raman scattering in the near field. This provides a platform to measure the vibrational modes or phonons of materials near the atomic scale. With an initial focus on molecular systems, various low temperature UHV-TERS studies have shown intramolecular (angstrom-scale) resolution of individual vibrational modes within a single molecule, and in some cases, even shown sensitivity to the formation or dissociation of a single chemical bond.[41, 162-166] Comparatively, UHV-TERS studies of materials have focused on slightly larger scales, detecting and identifying distinct phases. But a few early studies have demonstrated the ability to detect and identify atomic defects

as well as the effects of adsorption or chemisorption of individual chemical species. Furthermore, TERS in ambient conditions has recently been used to study low-angle twisted bilayer graphene[167] and mixed heterostructures.[104] Comparatively, this avenue remains currently unexplored with UHV-TERS, perhaps due to a degree of technical incompatibility with fabrication methods for these materials. However, the ability to probe highly sensitive phonon modes at the angstrom-scale in these and other newly designed materials offers tremendous potential once these obstacles are surmounted. Finally, thus far most UHV-TERS studies have been focused on steady-state measurements. However, the use of pulsed laser sources in the future offers the ability to capture dynamic processes[168, 169] as has been demonstrated with ultrafast surface-enhanced Raman spectroscopy.[170]

Scanning tunneling microscope induced luminescence (STML) uses an inelastic electron tunneling process or the injection of hot electrons to excite light emission at the STM junction. As shown in the discussed studies, this allows the precise spectral identification of emission down to a single atom or defect. Time correlated measurements provide a method to differentiate between the different mechanisms as well as track energy flow. In this way the development of new detection schemes improves the flexibility of STML to consider dynamic processes with exceptional temporal resolution. Although STML measurements require that a molecule or material be decoupled from the underlying substrate to prevent quenching effects, the study of heterostructures with this technique remains limited, offering a possible future direction for this powerful technique.

While the studies mentioned here focused on the detection of visible light, infrared,[45, 171-173] THz,[174-180] and even longer wavelength radiation[181] has been effectively coupled into UHV scanning probe microscope junctions with various excitation and detection schemes.[23, 182-185] In this regard, these methods have led to studies of light–matter interactions with exceptional spatial, as well as temporal resolution. The ongoing development of these techniques continues to offer exciting new opportunities to examine both established and new materials.

ACKNOWLEDGMENTS

J. F. S. acknowledges a National Research Council Postdoctoral Fellowship. N.J. acknowledges support from National Science Foundation (CHE-1944796).

AUTHOR DECLARATIONS

CONFLICT OF INTEREST

The authors have no conflicts of interest to declare.

DATA AVAILABILITY

All data shown within this article has been previously published. Suitable references can be found in the corresponding figure captions.

REFERENCES

1. D. A. Bonnell, D. N. Basov, M. Bode, U. Diebold, S. V. Kalinin, V. Madhavan, L. Novotny, M. Salmeron, U. D. Schwarz and P. S. Weiss, Rev. Mod. Phys. **84**, 1343-1381 (2012).
2. X. Liu and M. C. Hersam, Adv. Mater. **30**, 1801586 (2018).
3. G. R. Bhimanapati, Z. Lin, V. Meunier, Y. Jung, J. Cha, S. Das, D. Xiao, Y. Son, M. S. Strano, V. R. Cooper, L. Liang, S. G. Louie, E. Ringe, W. Zhou, S. S. Kim, R. R. Naik, B. G. Sumpter, H. Terrones, F. Xia, Y. Wang, J. Zhu, D. Akinwande, N. Alem, J. A. Schuller, R. E. Schaak, M. Terrones and J. A. Robinson, ACS Nano **9**, 11509-11539 (2015).

4. K. S. Novoselov, A. K. Geim, S. V. Morozov, D. Jiang, Y. Zhang, S. V. Dubonos, I. V. Grigorieva and A. A. Firsov, Science **306**, 666-669 (2004).
5. A. J. Mannix, B. Kiraly, M. C. Hersam and N. P. Guisinger, Nat. Rev. Chem. **1**, 0014 (2017).
6. A. McCreary, O. Kazakova, D. Jariwala and Z. Y. Al Balushi, 2D Mater. **8**, 013001 (2020).
7. K. S. Novoselov, A. Mishchenko, A. Carvalho and A. H. C. Neto, Science **353**, aac9439 (2016).
8. R. Mas-Ballesté, C. Gómez-Navarro, J. Gómez-Herrero and F. Zamora, Nanoscale **3**, 20-30 (2011).
9. X. Chen, D. Hu, R. Mescall, G. You, D. N. Basov, Q. Dai and M. Liu, Adv. Mater. **31**, 1804774 (2019).
10. D. Rhodes, S. H. Chae, R. Ribeiro-Palau and J. Hone, Nat. Mater. **18**, 541-549 (2019).
11. G. Binnig, H. Rohrer, C. Gerber and E. Weibel, Phys. Rev. Lett. **49**, 57-61 (1982).
12. J. Tersoff and D. R. Hamann, Phys. Rev. B **31**, 805-813 (1985).
13. L. Gross, Nat. Chem. **3**, 273-278 (2011).
14. E. Abbe, Arch. Mikrosk. Anat. **9**, 413-468 (1873).
15. J. F. Schultz, S. Li, S. Jiang and N. Jiang, J. Phys.: Condens. Matter **32**, 463001 (2020).
16. E. H. Synge, Philos. Mag. **6**, 356-362 (1928).
17. E. A. Ash and G. Nicholls, Nature **237**, 510-512 (1972).
18. D. W. Pohl, W. Denk and M. Lanz, Appl. Phys. Lett. **44**, 651-653 (1984).
19. D. W. Pohl, in *Near Field Optics*, edited by D. W. Pohl and D. Courjon (Springer Netherlands, Dordrecht, 1993), pp. 1-5.
20. H. Heinzelmann and D. W. Pohl, Appl. Phys. A **59**, 89-101 (1994).
21. W. M. Duncan, J. Vac. Sci. Technol., A **14**, 1914-1918 (1996).
22. J. Peng, S. Sokolov, D. Hernangómez-Pérez, F. Evers, L. Gross, J. M. Lupton and J. Repp, Science **373**, 452-456 (2021).
23. R. Gutzler, M. Garg, C. R. Ast, K. Kuhnke and K. Kern, Nat. Rev. Phys. **3**, 441-453 (2021).
24. R. Beams, L. G. Cançado and L. Novotny, Nano Lett. **11**, 1177-1181 (2011).
25. C. Girard and A. Dereux, Rep. Prog. Phys. **59**, 657-699 (1996).
26. A. Lewis, M. Isaacson, A. Harootunian and A. Muray, Ultramicroscopy **13**, 227-231 (1984).
27. E. Betzig, A. Lewis, A. Harootunian, M. Isaacson and E. Kratschmer, Biophys. J. **49**, 269-279 (1986).
28. D. Courjon, K. Sarayeddine and M. Spajer, Optics Communications **71**, 23-28 (1989).
29. R. C. Reddick, R. J. Warmack and T. L. Ferrell, Phys. Rev. B **39**, 767-770 (1989).
30. D. Zeisel, V. Deckert, R. Zenobi and T. Vo-Dinh, Chem. Phys. Lett. **283**, 381-385 (1998).
31. C. E. Jordan, S. J. Stranick, R. R. Cavanagh, L. J. Richter and D. B. Chase, Surf. Sci. **433-435**, 48-52 (1999).
32. K. Minn, B. Birmingham and Z. Zhang, J. Vac. Sci. Technol., A **38**, 030801 (2020).

33. W. Zhang, Z. Fang and X. Zhu, Chem. Rev. **117**, 5095-5109 (2017).
34. S. Kim, N. Yu, X. Ma, Y. Zhu, Q. Liu, M. Liu and R. Yan, Nat. Photonics **13**, 636-643 (2019).
35. R. D. Grober, T. D. Harris, J. K. Trautman and E. Betzig, Rev. Sci. Instrum. **65**, 626-631 (1994).
36. Y. Durand, J. C. Woehl, B. Viellerobe, W. Göhde and M. Orrit, Rev. Sci. Instrum. **70**, 1318-1325 (1999).
37. N. Jiang, E. T. Foley, J. M. Klingsporn, M. D. Sonntag, N. A. Valley, J. A. Dieringer, T. Seideman, G. C. Schatz, M. C. Hersam and R. P. Van Duyne, Nano Lett. **12**, 5061-5067 (2012).
38. E. A. Pozzi, G. Goubert, N. Chiang, N. Jiang, C. T. Chapman, M. O. McAnally, A.-I. Henry, T. Seideman, G. C. Schatz, M. C. Hersam and R. P. V. Duyne, Chem. Rev. **117**, 4961-4982 (2017).
39. I. C. Moldovan-Doyen, G. Xu, L. Greusard, G. Sevin, E. Strupiechonski, G. Beaudoin, I. Sagnes, S. P. Khanna, E. H. Linfield, A. G. Davies, R. Colombelli and Y. D. Wilde, Appl. Phys. Lett. **98**, 231112 (2011).
40. P. J. Whiteman, J. F. Schultz, Z. D. Porach, H. Chen and N. Jiang, J. Phys. Chem. C **122**, 5489-5495 (2018).
41. R. Zhang, Y. Zhang, Z. C. Dong, S. Jiang, C. Zhang, L. G. Chen, L. Zhang, Y. Liao, J. Aizpurua, Y. Luo, J. L. Yang and J. G. Hou, Nature **498**, 82-86 (2013).
42. S. Sheng, W. Li, J. Gou, P. Cheng, L. Chen and K. Wu, Rev. Sci. Instrum. **89**, 053107 (2018).
43. N. Tallarida, L. Rios, V. A. Apkarian and J. Lee, Nano Lett. **15**, 6386-6394 (2015).
44. S. Liu, M. Müller, Y. Sun, I. Hamada, A. Hammud, M. Wolf and T. Kumagai, Nano Lett. **19**, 5725-5731 (2019).
45. M. M. Qazilbash, M. Brehm, B.-G. Chae, P.-C. Ho, G. O. Andreev, B.-J. Kim, S. J. Yun, A. V. Balatsky, M. B. Maple, F. Keilmann, H.-T. Kim and D. N. Basov, Science **318**, 1750-1753 (2007).
46. D. L. Jeanmaire and R. P. Vanduyne, J. Electroanal. Chem. **84**, 1-20 (1977).
47. M. Fleischmann, P. J. Hendra and A. J. Mcquillan, Chem. Phys. Lett. **26**, 163-166 (1974).
48. M. G. Albrecht and J. A. Creighton, J. Am. Chem. Soc. **99**, 5215-5217 (1977).
49. P. L. Stiles, J. A. Dieringer, N. C. Shah and R. P. V. Duyne, Annu. Rev. Anal. Chem. **1**, 601-626 (2008).
50. D. W. Pohl, in *Advances in Optical and Electron Microscopy*, edited by T. Mulvey and C. J. R. Sheppard (Elsevier, 1991), Vol. 12, pp. 243-312.
51. S. Nie and S. R. Emory, Science **275**, 1102-1106 (1997).
52. A. B. Zrimsek, N. Chiang, M. Mattei, S. Zaleski, M. O. McAnally, C. T. Chapman, A. I. Henry, G. C. Schatz and R. P. Van Duyne, Chem. Rev. **117**, 7583-7613 (2017).
53. A. B. Zrimsek, N. L. Wong and R. P. Van Duyne, J. Phys. Chem. C **120**, 5133-5142 (2016).
54. E. A. Sprague-Klein, M. O. McAnally, D. V. Zhdanov, A. B. Zrimsek, V. A. Apkarian, T. Seideman, G. C. Schatz and R. P. Van Duyne, J. Am. Chem. Soc. **139**, 15212-15221 (2017).

55. J. Wessel, J. Opt. Soc. Am. B: Opt. Phys. **2**, 1538-1541 (1985).
56. J. Steidtner and B. Pettinger, Rev. Sci. Instrum. **78**, 103104 (2007).
57. J. Steidtner and B. Pettinger, Phys. Rev. Lett. **100**, 236101 (2008).
58. R. Saito, M. Hofmann, G. Dresselhaus, A. Jorio and M. S. Dresselhaus, Adv. Phys. **60**, 413-550 (2011).
59. J. Wu and L. Xie, Anal. Chem. **91**, 468-481 (2019).
60. F. Shao and R. Zenobi, Anal. Bioanal. Chem. **411**, 37-61 (2019).
61. A. Shiotari, T. Kumagai and M. Wolf, J. Phys. Chem. C **118**, 11806-11812 (2014).
62. L. Grill, M. Dyer, L. Lafferentz, M. Persson, M. V. Peters and S. Hecht, Nat. Nanotechnol. **2**, 687-691 (2007).
63. J. F. Schultz, B. Yang and N. Jiang, Nanoscale **12**, 2726-2731 (2020).
64. J. F. Schultz, B. Yang and N. Jiang, J. Chem. Phys. **154**, 044703 (2021).
65. Q. Fan, J. M. Gottfried and J. Zhu, Acc. Chem. Res. **48**, 2484-2494 (2015).
66. J. Cai, P. Ruffieux, R. Jaafar, M. Bieri, T. Braun, S. Blankenburg, M. Muoth, A. P. Seitsonen, M. Saleh, X. Feng, K. Mullen and R. Fasel, Nature **466**, 470-473 (2010).
67. S. Blankenburg, J. Cai, P. Ruffieux, R. Jaafar, D. Passerone, X. Feng, K. Müllen, R. Fasel and C. A. Pignedoli, ACS Nano **6**, 2020-2025 (2012).
68. J. M. Klingsporn, N. Jiang, E. A. Pozzi, M. D. Sonntag, D. Chulhai, T. Seideman, L. Jensen, M. C. Hersam and R. P. V. Duyne, J. Am. Chem. Soc. **136**, 3881-3887 (2014).
69. Y. Zhang, B. Yang, A. Ghafoor, Y. Zhang, Y.-F. Zhang, R.-P. Wang, J.-L. Yang, Y. Luo, Z.-C. Dong and J. G. Hou, Natl. Sci. Rev. **6**, 1169-1175 (2019).
70. J. Lee, K. T. Crampton, N. Tallarida and V. A. Apkarian, Nature **568**, 78-82 (2019).
71. M. Liao, S. Jiang, C. Hu, R. Zhang, Y. Kuang, J. Zhu, Y. Zhang and Z. Dong, Nano Lett. **16**, 4040-4046 (2016).
72. L. Li, J. F. Schultz, S. Mahapatra, X. Liu, C. Shaw, X. Zhang, M. C. Hersam and N. Jiang, J. Am. Chem. Soc. **143**, 15624-15634 (2021).
73. K. T. Crampton, J. Lee and V. A. Apkarian, ACS Nano **13**, 6363-6371 (2019).
74. L. Li, J. F. Schultz, S. Mahapatra, Z. Lu, X. Zhang and N. Jiang, Nat. Commun. **13**, 1796 (2022).
75. J. F. Schultz, L. Li, S. Mahapatra and N. Jiang, J. Phys.: Condens. Matter **34**, 204008 (2022).
76. T. Deckert-Gaudig, A. Taguchi, S. Kawata and V. Deckert, Chem. Soc. Rev. **46**, 4077-4110 (2017).
77. L. Langelüddecke, P. Singh and V. Deckert, Appl. Spectrosc. **69**, 1357-1371 (2015).
78. D. Kurouski, A. Dazzi, R. Zenobi and A. Centrone, Chem. Soc. Rev. **49**, 3315-3347 (2020).
79. R. Zenobi, Chem. Rev. **117**, 4943-4944 (2017).
80. J. F. Schultz, S. Mahapatra, L. Li and N. Jiang, Appl. Spectrosc. **74**, 1313-1340 (2020).
81. S. Mahapatra, Y. Ning, J. F. Schultz, L. Li, J.-L. Zhang and N. Jiang, Nano Lett. **19**, 3267-3272 (2019).
82. B. J. Feng, Z. J. Ding, S. Meng, Y. G. Yao, X. Y. He, P. Cheng, L. Chen and K. H. Wu, Nano Lett. **12**, 3507-3511 (2012).

83. G. Kukucska, V. Zolyomi and J. Koltai, Phys. Rev. B **98** (2018).
84. D. Solonenko, O. D. Gordan, G. L. Lay, H. Şahin, S. Cahangirov, D. R. T. Zahn and P. Vogt, 2D Mater. **4** (2016).
85. A. D. Alvarez, T. Zhu, J. P. Nys, M. Berthe, M. Empis, J. Schreiber, B. Grandidier and T. Xu, Surf. Sci. **653**, 92-96 (2016).
86. D. Solonenko, O. D. Gordan, G. Le Lay, D. R. T. Zahn and P. Vogt, Beilstein J. Nanotech. **8**, 1357-1365 (2017).
87. S. Sheng, J.-b. Wu, X. Cong, W. Li, J. Gou, Q. Zhong, P. Cheng, P.-h. Tan, L. Chen and K. Wu, Phys. Rev. Lett. **119**, 196803 (2017).
88. M. D. Mansour, R. Parret and L. Masson, J. Vac. Sci. Technol., A **36**, 061402 (2018).
89. C. Leandri, G. L. Lay, B. Aufray, C. Girardeaux, J. Avila, M. E. Dávila, M. C. Asensio, C. Ottaviani and A. Cricenti, Surf. Sci. **574**, L9-L15 (2005).
90. R. Bernard, T. Leoni, A. Wilson, T. Lelaidier, H. Sahaf, E. Moyen, L. Assaud, L. Santinacci, F. Leroy, F. Cheynis, A. Ranguis, H. Jamgotchian, C. Becker, Y. Borensztein, M. Hanbücken, G. Prévot and L. Masson, Phys. Rev. B **88**, 121411 (2013).
91. G. Prévot, C. Hogan, T. Leoni, R. Bernard, E. Moyen and L. Masson, Phys. Rev. Lett. **117**, 276102 (2016).
92. S. Sheng, R. Ma, J.-b. Wu, W. Li, L. Kong, X. Cong, D. Cao, W. Hu, J. Gou, J.-W. Luo, P. Cheng, P.-H. Tan, Y. Jiang, L. Chen and K. Wu, Nano Lett. **18**, 2937-2942 (2018).
93. S. Sheng, J.-B. Wu, X. Cong, Q. Zhong, W. Li, W. Hu, J. Gou, P. Cheng, P.-H. Tan, L. Chen and K. Wu, ACS Nano **13**, 4133-4139 (2019).
94. A. J. Mannix, X. F. Zhou, B. Kiraly, J. D. Wood, D. Alducin, B. D. Myers, X. L. Liu, B. L. Fisher, U. Santiago, J. R. Guest, M. J. Yacaman, A. Ponce, A. R. Oganov, M. C. Hersam and N. P. Guisinger, Science **350**, 1513-1516 (2015).
95. B. J. Feng, J. Zhang, Q. Zhong, W. B. Li, S. Li, H. Li, P. Cheng, S. Meng, L. Chen and K. H. Wu, Nat. Chem. **8**, 564-569 (2016).
96. R. Wu, I. K. Drozdov, S. Eltinge, P. Zahl, S. Ismail-Beigi, I. Bozovic and A. Gozar, Nat. Nanotechnol. **14**, 44-49 (2019).
97. A. P. Sergeeva, I. A. Popov, Z. A. Piazza, W.-L. Li, C. Romanescu, L.-S. Wang and A. I. Boldyrev, Acc. Chem. Res. **47**, 1349-1358 (2014).
98. Z. Zhang, Y. Yang, E. S. Penev and B. I. Yakobson, Adv. Funct. Mater. **27**, 1605059 (2017).
99. Z.-Q. Wang, T.-Y. Lü, H.-Q. Wang, Y. P. Feng and J.-C. Zheng, Front. Phys. **14**, 33403 (2019).
100. B. Feng, J. Zhang, Q. Zhong, W. Li, S. Li, H. Li, P. Cheng, S. Meng, L. Chen and K. Wu, Nat. Chem. **8**, 563-568 (2016).
101. B. Liu, Q. Liao, X. Zhang, J. Du, Y. Ou, J. Xiao, Z. Kang, Z. Zhang and Y. Zhang, ACS Nano **13**, 9057-9066 (2019).
102. Y. Han, K. Nguyen, M. Cao, P. Cueva, S. Xie, M. W. Tate, P. Purohit, S. M. Gruner, J. Park and D. A. Muller, Nano Lett. **18**, 3746-3751 (2018).
103. R. Beams, L. G. Cançado, A. Jorio, A. N. Vamivakas and L. Novotny, Nanotechnology **26**, 175702 (2015).
104. M. Rahaman, R. D. Rodriguez, G. Plechinger, S. Moras, C. Schüller, T. Korn and D. R. T. Zahn, Nano Lett. **17**, 6027-6033 (2017).

105. T.-a. Yano, T. Ichimura, S. Kuwahara, F. H'Dhili, K. Uetsuki, Y. Okuno, P. Verma and S. Kawata, Nat. Commun. **4**, 2592 (2013).
106. P. Hermann, M. Hecker, D. Chumakov, M. Weisheit, J. Rinderknecht, A. Shelaev, P. Dorozhkin and L. M. Eng, Ultramicroscopy **111**, 1630-1635 (2011).
107. A. Tarun, N. Hayazawa and S. Kawata, Anal. Bioanal. Chem. **394**, 1775-1785 (2009).
108. X. Liu, Z. Wei, I. Balla, A. J. Mannix, N. P. Guisinger, E. Luijten and M. C. Hersam, Sci. Adv. **3**, e1602356 (2017).
109. X. Liu and M. C. Hersam, Sci. Adv. **5**, eaax6444 (2019).
110. Q. Li, X. Liu, E. B. Aklile, S. Li and M. C. Hersam, Nano Lett. **21**, 4029-4035 (2021).
111. M. F. Crommie, C. P. Lutz and D. M. Eigler, Science **262**, 218-220 (1993).
112. J. A. Stroscio and D. M. Eigler, Science **254**, 1319-1326 (1991).
113. L. Gross, F. Mohn, N. Moll, P. Liljeroth and G. Meyer, Science **325**, 1110-1114 (2009).
114. P. Hapala, G. Kichin, C. Wagner, F. S. Tautz, R. Temirov and P. Jelínek, Phys. Rev. B **90**, 085421 (2014).
115. N. Tallarida, J. Lee and V. A. Apkarian, ACS Nano **11**, 11393-11401 (2017).
116. R. L. M. Gieseking, J. Lee, N. Tallarida, V. A. Apkarian and G. C. Schatz, J. Phys. Chem. Lett. **9**, 3074-3080 (2018).
117. J. Lee, N. Tallarida, X. Chen, L. Jensen and V. A. Apkarian, Science Advances **4**, eaat5472 (2018).
118. A. Bhattarai, K. T. Crampton, A. G. Joly, L. Kovarik, W. P. Hess and P. Z. El-Khoury, J. Phys. Chem. Lett. **9**, 7105-7109 (2018).
119. A. Bhattarai and P. Z. El-Khoury, Chem. Commun. **53**, 7310-7313 (2017).
120. P. Liu, D. V. Chulhai and L. Jensen, ACS Nano **11**, 5094-5102 (2017).
121. S. Mahapatra, L. Li, J. F. Schultz and N. Jiang, J. Chem. Phys. **153**, 010902 (2020).
122. S. Liu, B. Cirera, Y. Sun, I. Hamada, M. Müller, A. Hammud, M. Wolf and T. Kumagai, Nano Lett. **20**, 5879-5884 (2020).
123. K. J. Savage, M. M. Hawkeye, R. Esteban, A. G. Borisov, J. Aizpurua and J. J. Baumberg, Nature **491**, 574-577 (2012).
124. H. Miranda, C. Rabelo, L. G. Cançado, T. L. Vasconcelos, B. S. Oliveira, F. Schulz, H. Lange, S. Reich, P. Kusch and A. Jorio, Phys. Rev. Res. **2**, 023408 (2020).
125. S. Liu, A. Hammud, M. Wolf and T. Kumagai, Nano Lett. **21**, 4057-4061 (2021).
126. R. D. Young, Phys. Today **24**, 42-49 (1971).
127. R. Young, J. Ward and F. Scire, Rev. Sci. Instrum. **43**, 999-1011 (1972).
128. J. Lambe and S. L. McCarthy, Phys. Rev. Lett. **37**, 923-925 (1976).
129. N. V. Smith and D. P. Woodruff, Prog. Surf. Sci. **21**, 295-370 (1986).
130. J. K. Gimzewski, B. Reihl, J. H. Coombs and R. R. Schlittler, Z. Phys. B: Condens. Matter **72**, 497-501 (1988).
131. K. Kuhnke, A. Kabakchiev, W. Stiepany, F. Zinser, R. Vogelgesang and K. Kern, Rev. Sci. Instrum. **81**, 113102 (2010).
132. H. U. Yang, E. Hebestreit, E. E. Josberger and M. B. Raschke, Rev. Sci. Instrum. **84**, 023701 (2013).
133. B. N. J. Persson and A. Baratoff, Phys. Rev. Lett. **68**, 3224-3227 (1992).

134. G. Schull, N. Néel, P. Johansson and R. Berndt, Phys. Rev. Lett. **102**, 057401 (2009).
135. C. C. Leon, A. Rosławska, A. Grewal, O. Gunnarsson, K. Kuhnke and K. Kern, Sci. Adv. **5**, eaav4986 (2019).
136. K. Kuhnke, C. Große, P. Merino and K. Kern, Chem. Rev. **117**, 5174-5222 (2017).
137. X. H. Qiu, G. V. Nazin and W. Ho, Science **299**, 542-546 (2003).
138. F. Rossel, M. Pivetta and W.-D. Schneider, Surf. Sci. Rep. **65**, 129-144 (2010).
139. B. Doppagne, M. C. Chong, E. Lorchat, S. Berciaud, M. Romeo, H. Bulou, A. Boeglin, F. Scheurer and G. Schull, Phys. Rev. Lett. **118**, 127401 (2017).
140. F.-F. Kong, X.-J. Tian, Y. Zhang, Y.-J. Yu, S.-H. Jing, Y. Zhang, G.-J. Tian, Y. Luo, J.-L. Yang, Z.-C. Dong and J. G. Hou, Nat. Commun. **12**, 1280 (2021).
141. R. Berndt, J. K. Gimzewski and P. Johansson, Phys. Rev. Lett. **67**, 3796-3799 (1991).
142. R. Berndt, J. K. Gimzewski and R. R. Schlittler, Ultramicroscopy **42-44**, 355-359 (1992).
143. R. Berndt, R. Gaisch, W. D. Schneider, J. K. Gimzewski, B. Reihl, R. R. Schlittler and M. Tschudy, Phys. Rev. Lett. **74**, 102-105 (1995).
144. G. V. Nazin, X. H. Qiu and W. Ho, Phys. Rev. Lett. **90**, 216110 (2003).
145. H. M. Benia, X. Lin, H. J. Gao, N. Nilius and H. J. Freund, J. Phys. Chem. C **111**, 10528-10533 (2007).
146. F. Stavale, N. Nilius and H.-J. Freund, J. Phys. Chem. Lett. **4**, 3972-3976 (2013).
147. F. Stavale, L. Pascua, N. Nilius and H.-J. Freund, J. Phys. Chem. C **117**, 10552-10557 (2013).
148. M. C. Chong, N. Afshar-Imani, F. Scheurer, C. Cardoso, A. Ferretti, D. Prezzi and G. Schull, Nano Lett. **18**, 175-181 (2018).
149. M. Koch, F. Ample, C. Joachim and L. Grill, Nat. Nanotechnol. **7**, 713-717 (2012).
150. B. Schuler, K. A. Cochrane, C. Kastl, E. S. Barnard, E. Wong, N. J. Borys, A. M. Schwartzberg, D. F. Ogletree, F. J. G. d. Abajo and A. Weber-Bargioni, Sci. Adv. **6**, eabb5988 (2020).
151. A. Rosławska, P. Merino, A. Grewal, C. C. Leon, K. Kuhnke and K. Kern, Nano Lett. **21**, 7221-7227 (2021).
152. B. Yang, G. Chen, A. Ghafoor, Y. Zhang, Y. Zhang, Y. Zhang, Y. Luo, J. Yang, V. Sandoghdar, J. Aizpurua, Z. Dong and J. G. Hou, Nat. Photonics **14**, 693-699 (2020).
153. F. Benz, M. K. Schmidt, A. Dreismann, R. Chikkaraddy, Y. Zhang, A. Demetriadou, C. Carnegie, H. Ohadi, B. de Nijs, R. Esteban, J. Aizpurua and J. J. Baumberg, Science **354**, 726-729 (2016).
154. A. Rosławska, C. C. Leon, A. Grewal, P. Merino, K. Kuhnke and K. Kern, ACS Nano **14**, 6366-6375 (2020).
155. A. Rosławska, P. Merino, C. Große, C. C. Leon, O. Gunnarsson, M. Etzkorn, K. Kuhnke and K. Kern, Nano Lett. **18**, 4001-4007 (2018).
156. A. Rosławska, P. Merino, C. C. Leon, A. Grewal, M. Etzkorn, K. Kuhnke and K. Kern, Nano Lett. **21**, 4577-4583 (2021).
157. P. Merino, A. Rosławska, C. Große, C. C. Leon, K. Kuhnke and K. Kern, Sci. Adv. **4**, eaap8349 (2018).

158. P. Merino, C. Große, A. Rosławska, K. Kuhnke and K. Kern, Nat. Commun. **6**, 8461 (2015).
159. C. C. Leon, O. Gunnarsson, D. G. de Oteyza, A. Rosławska, P. Merino, A. Grewal, K. Kuhnke and K. Kern, ACS Nano **14**, 4216-4223 (2020).
160. D. N. Basov, M. M. Fogler and F. J. García de Abajo, Science **354**, aag1992 (2016).
161. A. A. Khajetoorians, D. Wegner, A. F. Otte and I. Swart, Nat. Rev. Phys. **1**, 703-715 (2019).
162. J. Xu, X. Zhu, S. Tan, Y. Zhang, B. Li, Y. Tian, H. Shan, X. Cui, A. Zhao, Z. Dong, J. Yang, Y. Luo, B. Wang and J. G. Hou, Science **371**, 818-822 (2021).
163. H. Li, Y.-F. Zhang, X.-B. Zhang, A. Farrukh, Y. Zhang, Y. Zhang and Z.-C. Dong, J. Chem. Phys. **153**, 244201 (2020).
164. A. Ghafoor, B. Yang, Y.-j. Yu, Y.-f. Zhang, X.-b. Zhang, G. Chen, Y. Zhang, Y. Zhang and Z.-c. Dong, Chin. J. Chem. Phys. **32**, 287-291 (2019).
165. C. Zhang, R. B. Jaculbia, Y. Tanaka, E. Kazuma, H. Imada, N. Hayazawa, A. Muranaka, M. Uchiyama and Y. Kim, J. Am. Chem. Soc. **143**, 9461-9467 (2021).
166. R. B. Jaculbia, H. Imada, K. Miwa, T. Iwasa, M. Takenaka, B. Yang, E. Kazuma, N. Hayazawa, T. Taketsugu and Y. Kim, Nat. Nanotechnol. **15**, 105-110 (2020).
167. A. C. Gadelha, D. A. A. Ohlberg, C. Rabelo, E. G. S. Neto, T. L. Vasconcelos, J. L. Campos, J. S. Lemos, V. Ornelas, D. Miranda, R. Nadas, F. C. Santana, K. Watanabe, T. Taniguchi, B. van Troeye, M. Lamparski, V. Meunier, V.-H. Nguyen, D. Paszko, J.-C. Charlier, L. C. Campos, L. G. Cançado, G. Medeiros-Ribeiro and A. Jorio, Nature **590**, 405-409 (2021).
168. E. A. Pozzi, M. D. Sonntag, N. Jiang, N. Chiang, T. Seideman, M. C. Hersam and R. P. Van Duyne, J. Phys. Chem. Lett. **5**, 2657-2661 (2014).
169. M. J. Feldstein, P. Vöhringer, W. Wang and N. F. Scherer, J. Phys. Chem. **100**, 4739-4748 (1996).
170. N. L. Gruenke, M. F. Cardinal, M. O. McAnally, R. R. Frontiera, G. C. Schatz and R. P. Van Duyne, Chem. Soc. Rev. **45**, 2263-2290 (2016).
171. A. S. McLeod, E. van Heumen, J. G. Ramirez, S. Wang, T. Saerbeck, S. Guenon, M. Goldflam, L. Anderegg, P. Kelly, A. Mueller, M. K. Liu, I. K. Schuller and D. N. Basov, Nat. Phys. **13**, 80-86 (2017).
172. Z. Fei, G. O. Andreev, W. Bao, L. M. Zhang, A. S. McLeod, C. Wang, M. K. Stewart, Z. Zhao, G. Dominguez, M. Thiemens, M. M. Fogler, M. J. Tauber, A. H. Castro-Neto, C. N. Lau, F. Keilmann and D. N. Basov, Nano Lett. **11**, 4701-4705 (2011).
173. M. Garg, A. Martin-Jimenez, Y. Luo and K. Kern, ACS Nano **15**, 18071-18084 (2021).
174. T. L. Cocker, V. Jelic, R. Hillenbrand and F. A. Hegmann, Nat. Photonics **15**, 558-569 (2021).
175. S. E. Ammerman, V. Jelic, Y. Wei, V. N. Breslin, M. Hassan, N. Everett, S. Lee, Q. Sun, C. A. Pignedoli, P. Ruffieux, R. Fasel and T. L. Cocker, Nat. Commun. **12**, 6794 (2021).
176. T. L. Cocker, D. Peller, P. Yu, J. Repp and R. Huber, Nature **539**, 263-267 (2016).

177. T. L. Cocker, V. Jelic, M. Gupta, S. J. Molesky, J. A. J. Burgess, G. D. L. Reyes, L. V. Titova, Y. Y. Tsui, M. R. Freeman and F. A. Hegmann, Nat. Photonics **7**, 620-625 (2013).
178. M. Garg and K. Kern, Science **367**, 411-415 (2020).
179. K. Kimura, Y. Morinaga, H. Imada, I. Katayama, K. Asakawa, K. Yoshioka, Y. Kim and J. Takeda, ACS Photonics **8**, 982-987 (2021).
180. V. Jelic, K. Iwaszczuk, P. H. Nguyen, C. Rathje, G. J. Hornig, H. M. Sharum, J. R. Hoffman, M. R. Freeman and F. A. Hegmann, Nat. Phys. **13**, 591-598 (2017).
181. S. Baumann, W. Paul, T. Choi, C. P. Lutz, A. Ardavan and A. J. Heinrich, Science **350**, 417-420 (2015).
182. M. Völcker, W. Krieger and H. Walther, AIP Conf. Proc. **241**, 51-60 (1991).
183. W. Ho, J. Chem. Phys. **117**, 11033-11061 (2002).
184. S. Wieghold and L. Nienhaus, Joule **4**, 524-538 (2020).
185. G. Dai, Z. Yang, G. Geng, M. Li, T. Chang, D. Wei, C. Du, H.-L. Cui and H. Wang, Appl. Spectrosc. Rev. **53**, 806-835 (2018).